Check for updates

JGR Atmospheres

RESEARCH ARTICLE
10.1029/2025JD044464

Storms Generated by a Sharp Vegetation Contrast Between Huge Irrigated Oasis and Adjacent Desert

Quxin Cui[1], Zhiyong Meng[1], Yiren Lin[2], Yipeng Huang[3], Zimeng Zheng[1], Xiaojuan Yao[4], Yonggang Sun[5], and Xuefeng Meng[4]

[1]Department of Atmospheric and Oceanic Sciences, School of Physics, and China Meteorological Administration Tornado Key Laboratory, Peking University, Beijing, China, [2]Department of Astronomy, School of Physics, Peking University, Beijing, China, [3]Xiamen Key Laboratory of Straits Meteorology, Xiamen Meteorological Bureau, Xiamen, China, [4]Inner Mongolia Meteorological Observatory, Hohhot, China, [5]Inner Mongolia Climate Center, Hohhot, China

Abstract This work presents comprehensive observational evidence on how sharp vegetation contrasts between irrigated oases and deserts can affect local and regional weather. Hetao irrigation district, a 769,333-ha wide World Heritage Irrigation Structure in Inner Mongolia, China, illustrates how humanity's biggest hydraulic engineering project becomes a storm generator through enhancing vegetation contrast with its adjacent extensive deserts. Based on radar data collected during warm seasons from 2012 to 2023, this study explores the evolution, diurnal variation, organization, and movement of convective systems (CSs) initiated by boundary layer convergence lines that formed due to vegetation contrast between the irrigated oasis and adjacent Kubuqi and Ulan Buh deserts in different synoptic patterns in the Hetao area. A total of 228 CSs formed primarily along vegetation contrast lines in arid areas under synoptic patterns featuring adequate moisture and substantial instability, with ~35% exhibiting linear organization and ~20% propagating far downstream. These features were also compared across the borders between the Oasis and the Kubuqi Desert versus the Ulan Buh Desert, which have different sharpness of vegetation heterogeneity. Due to the sharper vegetation contrast, CSs over the Kubuqi Desert were nearly 11.7 times more prevalent with a higher prevalence of stronger linear organizational mode, greater intensity, and more frequent downstream propagation than those over the Ulan Buh Desert with a less sharp vegetation gradient, where stronger cellular organizational mode was dominant. These findings hold important implications for the nowcasting of severe weather in the semiarid Inner Mongolia and potentially in other desert-oasis border regions worldwide.

Plain Language Summary Surface vegetation differences across desert-oasis borders may cause severe storms that are a challenge to predict in arid and/or semiarid areas. This study provides the first real-world evidence of the behavior of deep convective storms generated by boundary layer convergence lines across desert-oasis borders using 12 years of radar observations in the Hetao area in Inner Mongolia, China. This area offers an unparalleled example of different vegetation divides between a huge irrigated oasis and extensive deserts. Storms are likely to occur in deserts with a sharp vegetation divide and those with a linear organization tend to move far downstream. The results can be useful for severe weather forecasting and early warning systems both locally and in other vulnerable arid and semiarid regions globally.

Key Points:

- Storms over the Kubuqi Desert were nearly 40 times more prevalent than over the Oasis
- Storms over the Kubuqi Desert were more frequent and better organized due to its sharper land use contrast than over other regions
- Two-fifths of the Kubuqi storms exhibited linear orientation and one-fifth moved far downstream

Correspondence to:

Z. Meng,
zymeng@pku.edu.cn

Citation:

Cui, Q., Meng, Z., Lin, Y., Huang, Y., Zheng, Z., Yao, X., et al. (2025). Storms generated by a sharp vegetation contrast between huge irrigated oasis and adjacent desert. *Journal of Geophysical Research: Atmospheres*, *130*, e2025JD044464. https://doi.org/10.1029/2025JD044464

Received 28 MAY 2025
Accepted 5 OCT 2025

Author Contributions:

Conceptualization: Zhiyong Meng
Data curation: Quxin Cui, Yiren Lin, Yipeng Huang, Zimeng Zheng, Xiaojuan Yao, Yonggang Sun, Xuefeng Meng
Formal analysis: Quxin Cui
Funding acquisition: Zhiyong Meng
Investigation: Quxin Cui, Zhiyong Meng
Methodology: Quxin Cui, Zhiyong Meng, Yiren Lin, Yipeng Huang
Project administration: Zhiyong Meng
Resources: Zhiyong Meng
Software: Quxin Cui
Supervision: Zhiyong Meng
Validation: Quxin Cui
Visualization: Quxin Cui
Writing – original draft: Quxin Cui
Writing – review & editing: Quxin Cui, Zhiyong Meng, Yiren Lin, Yipeng Huang, Zimeng Zheng, Xiaojuan Yao, Yonggang Sun, Xuefeng Meng

© 2025. American Geophysical Union. All Rights Reserved.

1. Introduction

Soil moisture and rainfall feedbacks play a crucial role in weather across many regions. Horizontal contrasts between dry and wet soil patches generate mesoscale circulations, which promote deep convection initiation (CI) preferentially on the downwind side of dry soil patches adjacent to wetter regions. Studies based on satellite data have highlighted the significance of soil moisture and vegetation heterogeneity in deep CI in Europe (Taylor, 2015), the United States (Yuan et al., 2020), West Africa (Taylor et al., 2011), South America (Chug et al., 2023), and Tibetan Plateau (Barton et al., 2021). However, limited evidence exists on the effects of vegetation differences across irrigated oases and deserts. The Hetao area in Inner Mongolia, China, presents an unparalleled example with a sharp vegetation divide between an extensive irrigated oasis and adjacent desert, frequently creating thunderstorms and even tornadoes in warm seasons (Meng et al., 2024).

The Hetao area, situated on the north side of the Yellow River bend, encompasses one of China's largest irrigated oases: the 2,200-year-old Hetao irrigation oasis, covering 769,333 ha (Figure 1). Designated as a World Heritage Irrigation Structure in 2019, the Hetao irrigation oasis has played a crucial role in China's grain and oil production.

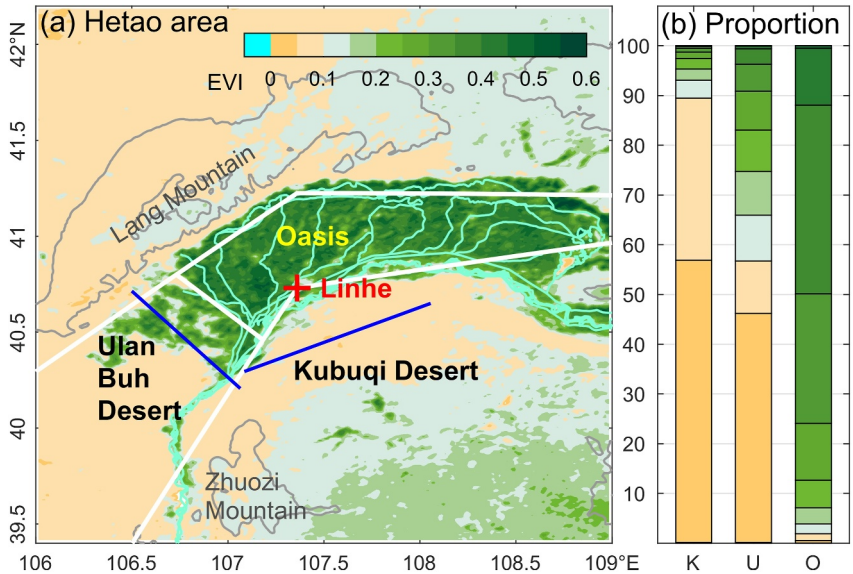

Figure 1. (a) Characteristics of the underlying surface in the Hetao area, shaded by the averaged enhanced vegetation index (EVI) during the warm seasons from 2012 to 2023. The red cross denotes the location of Linhe radar. The cyan curves represent the Yellow River, and the gray contours indicate terrain elevations of 1,500 m and 2,000 m above the mean sea level. The white lines delineate the borders of three subregions. The blue straight lines are the typical boundary layer convergence lines (BLCLs) over the Kubuqi Desert and the Ulan Buh Desert, respectively. (b) Proportions of EVI values over the Kubuqi Desert, the Ulan Buh Desert and the Oasis.

Surrounding this irrigated oasis are arid and semiarid lands, including the Kubuqi Desert to the southeast, the Ulan Buh Desert to the southwest, and Lang Mountain to the northwest, creating distinctive vegetation contrasts.

The Hetao area provides unique real-world evidence of how sharp vegetation contrasts can affect local and regional weather. Air over the irrigated oasis tends to be moister and cooler than the surrounding desert air (Kawase et al., 2008). When cooler air from the oasis meets warmer winds from the desert, an atmospheric boundary layer convergence line (BLCL hereafter) may form (Lee et al., 2019), often appearing as a fine line on radar imagery over dry surfaces as indicated by blue lines relative to the white subregional borders in Figure 1a. Along these BLCLs, if sufficient moisture and instability are present, CI may occur. Some of these initiated storms can travel long distances, causing destruction elsewhere. For example, the extreme rainfall in Beijing, China, on 21 July 2012—which resulted in 79 fatalities (Yu & Meng, 2016)—could be traced back to the Hetao area (X. Meng et al., 2013; Yu, 2012). Similarly, on 24 July 2022, a convective storm initiated by a BLCL generated a tornado over the Kubuqi Desert while propagating downstream (Meng et al., 2024). On the following day, 25 July 2022, a decaying convective storm reinitiated after interacting with a BLCL over the Kubuqi Desert. Occasionally, the BLCL extends northeastward over the Oasis, producing more severe weather in the eastern oasis than in the west (Meng et al., 2024)—a phenomenon that has been perplexing for local weather forecasters before the role of BLCLs was realized. Therefore, gaining a comprehensive understanding of the general features of BLCLs and their associated convective systems (CSs) is crucial for effective local and downstream disaster mitigation efforts.

According to Huang et al. (2019), an average of 60 summer days each year from 2012 to 2016 produced BLCLs, with 44% resulting in CI. Huang et al. (2022) classified the synoptic environments in warm seasons in the Hetao area into five patterns. They found that BLCLs are most likely to occur on warm summer days when the Hetao irrigation oasis is located ahead of a midlevel trough or on the western edge of the subtropical high, with southerly winds opposing the oasis breeze and higher temperatures over the desert than the oasis, creating optimal conditions in low-level humidity and instability. Using a real-world simulation, Liu et al. (2023) demonstrated that a BLCL initiated convection by lifting parcels from the southern low-level desert side and western midlevel oasis side rather than the low-level oasis side as suggested by idealized numerical simulations in the literature (Courault et al., 2007; Seth & Giorgi, 1996; Wang et al., 2011).

21698996, 2025, 20, Downloaded from https://agupubs.onlinelibrary.wiley.com/doi/10.1029/2025JD044464 by Peking University Health, Wiley Online Library on [03/12/2025]. See the Terms and Conditions (https://onlinelibrary.wiley.com/terms-and-conditions) on Wiley Online Library for rules of use; OA articles are governed by the applicable Creative Commons License

21698996, 2025, 20, Downloaded from https://agupubs.onlinelibrary.wiley.com/doi/10.1029/2025JD044464 by Peking University Health, Wiley Online Library on [03/12/2025]. See the Terms and Conditions (https://onlinelibrary.wiley.com/terms-and-conditions) on Wiley Online Library for rules of use; OA articles are governed by the applicable Creative Commons License

Although Huang et al. (2019) examined the frequency distribution of convective precipitation associated with BLCLs, characteristics of CSs induced by BLCLs over this sharp vegetation divide in the Hetao area, particularly their organizational modes which are strongly linked to severe weather impacts (Parker & Johnson, 2000), remain largely unknown. For example, are they predominantly linear due to the linear lifting mechanism? What fraction of these systems affects downstream regions? Do their features differ among different synoptic patterns and between the Kubuqi and Ulan Buh deserts with different vegetation-contrast sharpness?

Driven by these scientific questions, building upon previous studies on BLCL characteristics and their favorable synoptic patterns, this study aims to present the first real-world evidence illustrating behaviors of deep CSs associated with the sharp vegetation contrast between an irrigated oasis and the adjacent extensive deserts, based on radar data collected during 12 warm seasons from 2012 to 2023 in the Hetao area, revealing the organizational features of CSs that are not discernible from satellite data. Section 2 introduces data and methods. Section 3 provides the statistical characteristics of the CSs mainly over the two extensive deserts. A brief summary is given in Section 4.

2. Data and Methods

The vegetation heterogeneity of the underlying surface in the Hetao area was indicated by the enhanced vegetation index (EVI) derived from the Terra MODIS Vegetation Indices Monthly (MOD13A3) Version 6.1. EVI data were mosaicked and bilinearly interpolated to a 0.01° latitude and longitude grid for each month from June to August 2012–2023, using the MODIS Reprojection Tool (MRT) (Dwyer & Schmidt, 2006). A twelve-year-summer average was computed to derive the mean state of the underlying surface. Areas with EVI values less than 0.15 were classified as arid, while those with EVI values greater than 0.3 were considered vegetated (Huang et al., 2019) (Figure 1). The ASTER Global Digital Elevation Model (ASTGTM) Version 3 data, with a spatial resolution of 1 arc s, were mosaicked and interpolated to a 0.01° latitude and longitude grid, followed by smoothing using a nine-point smoothing method, representing the topography of the Hetao area.

Similar to Huang et al. (2019), data from the CD-band China New Generation Doppler Weather Radar at Linhe (located at the red cross in Figure 1a) were used from June to August 2012–2023. It has an unambiguous range of approximately 166.5 km and a data missing rate of 6%. Radar data were interpolated into a grid of $0.5 \times 0.5 \times 1$ km.

Convective cells were identified and tracked objectively using Thunderstorm Identification Tracking Analysis and Nowcasting (TITAN) (Dixon & Wiener, 1993). A convective cell is identified as the contiguous region with reflectivities of no less than 40 dBZ (Parker & Johnson, 2000), a volume of no less than 1 km^3, and a duration of at least 5 min. Convective cells within a distance of no more than 29 km from each other were grouped into CSs. If the CSs at adjacent times overlap in the area or have the closest distance between their edges within 18 km, they are regarded as belonging to one system. The criteria of 29 and 18 km yielded results that were most consistent with manual identification.

The features of CSs analyzed in this work were calculated within the radar range. A CS moving beyond the radar range without weakening is categorized as far downstream movement. Three stages in the lifespan of a CS associated with a BLCL were examined: (a) initiation stage: the first time its reflectivity reaches 30 dBZ; (b) maturity stage: the time when the envelope area of the composite reflectivity exceeding 40 dBZ is at its maximum; and (c) dissipation stage: the last time its 40 dBZ reflectivity occurs within the radar range.

BLCL cases from 2012 to 2016 were adopted from Huang et al. (2019) in which BLCLs were identified as radar fine lines with reflectivity values ranging from −5 to 10 dBZ and a minimum length of 10 km. The same identification method and criteria were used to identify BLCLs for the period 2017–2023. A CS was considered to be initiated by a specific BLCL if its first occurrence of 30-dBZ reflectivity was located within 50 km of the BLCL, following the distance threshold of Huang et al. (2019). Using these criteria, a total of 669 BLCLs were identified, among which 177 were associated with the initiation of CSs (Figure 2).

BLCLs were classified into three subregions—Kubuqi, Ulan Buh, and Oasis—according to the centroid positions at the time of CI (for convective BLCLs) or at the time of maximum length (for nonconvective BLCLs). Correspondingly, CSs were assigned to the same subregions based on the centroid positions of their associated BLCLs at the time of initiation. This classification facilitates the investigation of potential differences in the

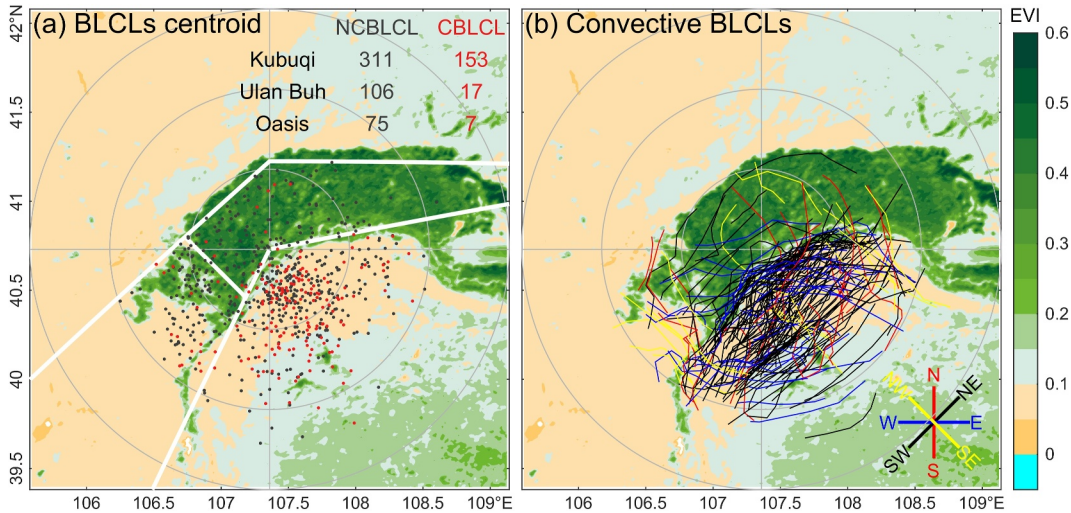

Figure 2. Spatial distribution of (a) the centroids of all 669 BLCLs identified during the summers of 2012–2023 and (b) the 177 convective BLCLs analyzed in this work at their CI stage superimposed on the averaged EVI (shaded) for the 2012–2023 warm seasons. In (a), black dots represent nonconvective BLCLs, while red dots denote convective BLCLs; white lines indicate the borders of three subregions as shown in Figure 1a. In (b), polylines in four different colors represent the BLCLs based on their orientation.

initiation and evolution of CSs over different underlying surfaces. In cases where a CS was initiated by multiple BLCLs whose centroids did not lie in the same geographical category, the system was classified as mixed.

In addition to the aforementioned geographical locations, we classified the CSs according to their synoptic patterns and organizational modes. Huang et al. (2022) classified the synoptic patterns into five categories, labeled T1 to T5 (Figure 3), based on the juxtaposition of the Hetao area relative to midlevel weather systems. T1 (in a high-pressure ridge), T4 (in front of a shallow midlevel trough), and T5 (in front of a deep midlevel trough) are favorable patterns for BLCL formation and CI, with T1 having the highest frequency. These three favorable patterns featured higher near surface temperature (Figures 3d1, 3d4, and 3d5) and thus higher CAPE (red box areas in Figures 3f1, 3f4, and 3f5) and temperature gradients across desert and oasis, and southerly winds over the Kubuqi Desert (Figures 3e1, 3e4, and 3e5) with rich moisture supply, enhancing the convergence with northerly oasis winds (Figures 3g1, 3g4, and 3g5). In contrast, T2 and T3, representing post midlevel shallow and deep troughs, respectively, with reduced occurrence of BLCL and associated CI, are considered unfavorable for BLCL formation and CI. These two unfavorable patterns featured lower near surface temperature (Figures 3d2 and 3d3) and thus lower CAPE (red box areas in Figures 3f2 and 3f3) and temperature gradients across desert and oasis, and northerly wind over the Kubuqi Desert (Figures 3e2 and 3e3) with much less moisture supply, hindering the formation of convergence (Figures 3g2 and 3g3). This synoptic classification method was based on MSLP rather than parameters directly related to convective development. In this framework, an "unfavorable synoptic pattern" indicates conditions generally unconducive to BLCLs and their CI rather than pure CSs. The sharp vegetation contrast mainly determines the formation and intensity of BLCL and thus the lifting mechanism in CI stage, while the development and movement of CSs are primarily controlled by the synoptic conditions.

The organizational modes of CSs were divided into six categories based on their morphologies and strength at the maturity stage (Figure 4). A CS is categorized as linear if the area covered by the composite reflectivity at or above 40 dBZ has a length-to-width aspect ratio of at least 3, in alignment with Meng and Zhang (2012) and Smith et al. (2012). A linear CS with a major axis length of at least 100 km is defined as a strong line (SL), akin to the length threshold outlined by Parker and Johnson (2000) and Houze (2004). Alternatively, a linear CS falling below this threshold is classified as a weak line (WL). A CS with a length-to-width ratio of less than 3 is designated as cellular if it comprises only one contiguous area of reflectivity of at least 40 dBZ; otherwise, it is labeled as clustered. Depending on whether the maximum reflectivity exceeds 50 dBZ or not, cellular and clustered CSs are further divided into strong cell (SCe) and weak cell (WCe), strong cluster (SCl) and weak cluster (WCl), respectively.

21698996, 2025, 20, Downloaded from https://agupubs.onlinelibrary.wiley.com/doi/10.1029/2025JD044464 by Peking University Health, Wiley Online Library on [03/12/2025]. See the Terms and Conditions (https://onlinelibrary.wiley.com/terms-and-conditions) on Wiley Online Library for rules of use; OA articles are governed by the applicable Creative Commons License

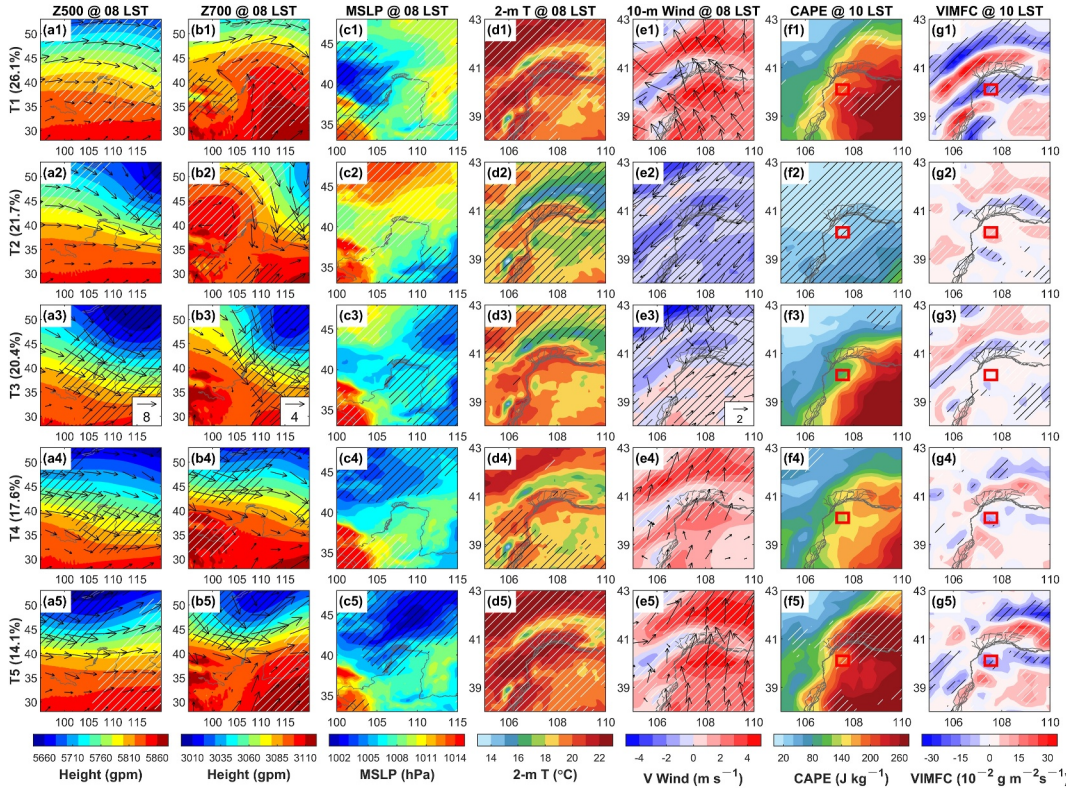

Figure 3. ERA5-based composite of (a) 500-hPa geopotential height (gpm) and wind (m s^{-1}), (b) 700-hPa geopotential height (gpm) and wind (m s^{-1}), (c) mean sea level pressure (hPa), (d) 2-m temperature (°C), (e) 10-m wind (m s^{-1}), at 0800 LST, (f) convective available potential energy (J kg^{-1}), and (g) vertically integrated moisture flux convergence (10^{-2} g m^{-2} s^{-1}) at 1000 LST, for the five synoptic patterns during warm seasons from 2012 to 2016. The occurrence frequencies of T1 to T5 are given on the left-hand side. The Yellow River is denoted by gray curves. The hatched areas in each panel indicate regions passing the Student's *t*-test at a confidence level of 90%. The red boxes denote the key areas of convection associated with BLCLs. This figure is adapted from Huang et al. (2022).

3. Statistical Characteristics of CSs

A total of 228 CSs associated with 177 BLCLs (26.5% of all BLCLs, Figure 2) were identified on 150 days out of 1,104 days (13.6%), with 21.1% of the CSs moving far downstream. CSs occurred more frequently in synoptic patterns T1 (40.7%), T5 (25.4%), and T4 (19.3%) due to favorable thermal, moisture, and instability conditions, but were less frequent in T3 (7.3%) and T2 (7.3%).

Rather than a dominant linear mode, the CSs associated with BLCLs exhibited a balanced morphology of linear, cellular, and clustered types (Figure 4), with the strong modes persisting longer, developing to higher altitudes, exhibiting larger mean reflectivity and precipitation areas in general, and being more likely to move far downstream (Figure 5).

Among the linear CSs, 61.7% were identified as weak lines and 38.3% were classified as strong lines. Despite the relatively low proportion of strong lines, they had the largest rate of downstream movement (68%). Strong lines were particularly prevalent in T5 (Figure 6a), where the Hetao area lies in front of a deep 500 hPa trough, characterized by strong southerly 10-m winds that accumulate water vapor and high CAPE (the last row in Figure 3). Other organizational modes with a relatively high proportion of downstream movement, that is, strong cluster and weak line (36% and 12% of which move downstream, respectively), also exhibited a large proportion for T5 only second to T1 (Figure 6a), which made strong line, weak line, and strong cluster become the top three modes in T5 (Figure 6b). The vast majority of cellular CSs dissipated within the radar range (Figures 4b and 4e).

Given that CSs associated with BLCLs over different underlying surfaces may exhibit distinct features, we analyzed the statistical characteristics of CSs over different underlying surfaces.

21698996, 2025, 20, Downloaded from https://agupubs.onlinelibrary.wiley.com/doi/10.1029/2025JD044464 by Peking University Health, Wiley Online Library on [03/12/2025]. See the Terms and Conditions (https://onlinelibrary.wiley.com/terms-and-conditions) on Wiley Online Library for rules of use; OA articles are governed by the applicable Creative Commons License

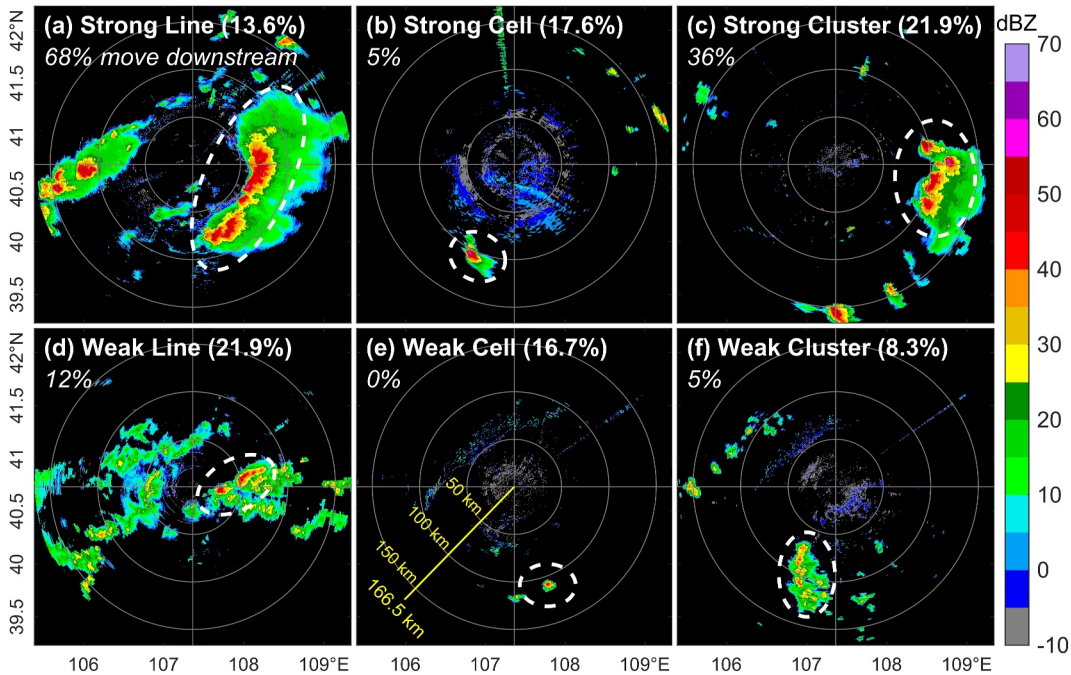

Figure 4. (a–f) Exemplars of the six organizational modes depicted in radar composite reflectivity. The percentages in parentheses indicate the proportion of corresponding organizational modes and the percentages in italics represent the proportion of CSs of the corresponding modes moving far downstream. The white dashed circles highlight the focused CSs, and the timestamp for each case is as follows: 1457 LST 21 July 2013; 1520 LST 15 August 2021; 1821 LST 29 July 2022; 1751 LST 14 August 2020; 1217 LST 23 July 2016; 1415 LST 14 July 2019.

3.1. CSs Over the Kubuqi Desert

Kubuqi contributed to 87.3% of the CSs associated with BLCLs in the Hetao area, approximately 40 times more than those in the Oasis (Figure 7). This predominance can be attributed in part to the higher frequency of BLCL occurrences over the Kubuqi Desert (464 BLCLs, Figure 2a) which was roughly six times the number observed over the Oasis. Less favorable conditions over the Oasis compared to those over the desert contributed to its lower incidence of convective activity. Large-scale subsidence over the Oasis due to more vegetation coverage (Figure 1) likely inhibited convection, as evidenced by the fact that nearly one third of the BLCLs over the Kubuqi Desert were convective, whereas only 8.5% of those over the Oasis exhibited convective characteristics. The lower proportion of convective BLCLs than in Huang et al. (2019) was due to the severe threshold for CSs identification in this study. Moreover, CSs in the Kubuqi subregion tended to occur in synoptic patterns that were more favorable for convection (Figures 6b and 7), namely T1 (44.2%), T5 (22.6%), and T4 (19.1%), aligning with the overall distribution.

The proportions of different organizational modes among Kubuqi CSs were balanced (Figure 7), with weak line accounting for the largest share (23.6%), followed by strong cluster (21.6%). Of the 199 CSs over the Kubuqi Desert, 29 were classified as strong line, accounting for 93.6% of all strong line CSs in the Hetao area and contributing to a higher percentage of far downstream movement (21.6%) in this subregion than that (21.1%) of all samples.

All six organizational modes were present across the five synoptic patterns, albeit in varying proportions (Figure 6b). Linear modes, particularly strong line, were predominantly observed in T5 and T1. Cellular modes, especially strong cell, were more commonly found in T1 and T4. Clustered modes primarily occurred in T1, with similar frequencies in T5 and T4. A higher proportion of CSs moved far downstream in T3 (33%) and T5 (24%) compared to T1, T2, and T4, each of which had around 20% of cases developing downstream.

The highest proportion for downstream movement in T3 is possibly owing to its strongest midlevel northwesterly wind (Table 1) and large CAPE in the downstream area (Figure 3f3). In this pattern, BLCL and CI are hard to occur because the environmental wind is in the same direction as the oasis wind and thus is not favorable for the

21698996, 2025, 20, Downloaded from https://agupubs.onlinelibrary.wiley.com/doi/10.1029/2025JD044464 by Peking University Health, Wiley Online Library on [03/12/2025]. See the Terms and Conditions (https://onlinelibrary.wiley.com/terms-and-conditions) on Wiley Online Library for rules of use; OA articles are governed by the applicable Creative Commons License

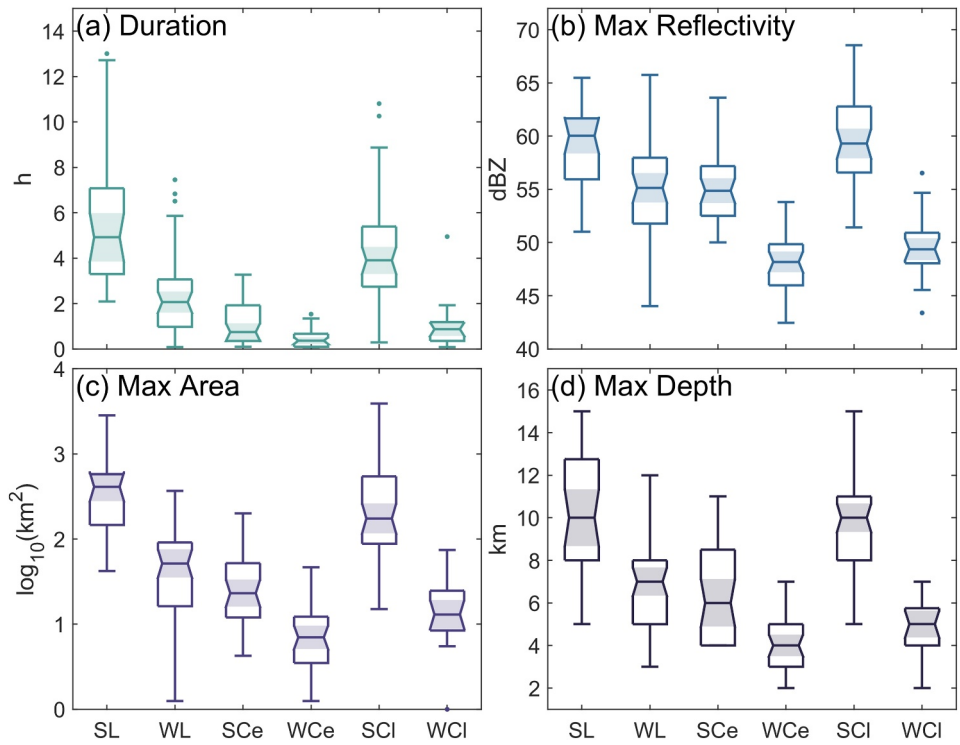

Figure 5. Box-and-whisker plots of (a) duration, (b) maximum reflectivity, (c) maximum area, and (d) maximum depth of CSs, categorized by organizational modes. The central horizontal line inside each box indicates the median; the top and bottom edges of each box represent the 25th and 75th percentiles; whiskers denote the minimum and maximum values excluding outliers; and dots indicate outliers.

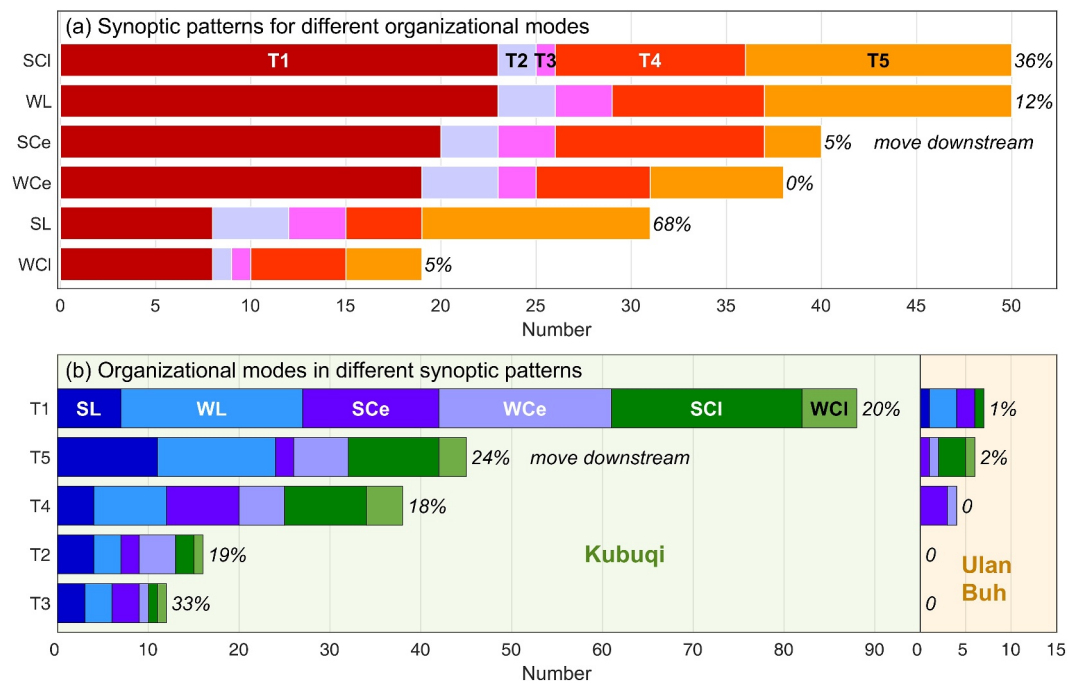

Figure 6. (a) Number of synoptic patterns for each organizational mode. (b) Number of CSs by synoptic patterns associated with BLCLs over the Kubuqi Desert and the Ulan Buh Desert. Percentages in italics next to the bars in (a) and (b) represent the proportion of CSs that moved far downstream.

21698996, 2025, 20, Downloaded from https://agupubs.onlinelibrary.wiley.com/doi/10.1029/2025JD044464 by Peking University Health, Wiley Online Library on [03/12/2025]. See the Terms and Conditions (https://onlinelibrary.wiley.com/terms-and-conditions) on Wiley Online Library for rules of use; OA articles are governed by the applicable Creative Commons License

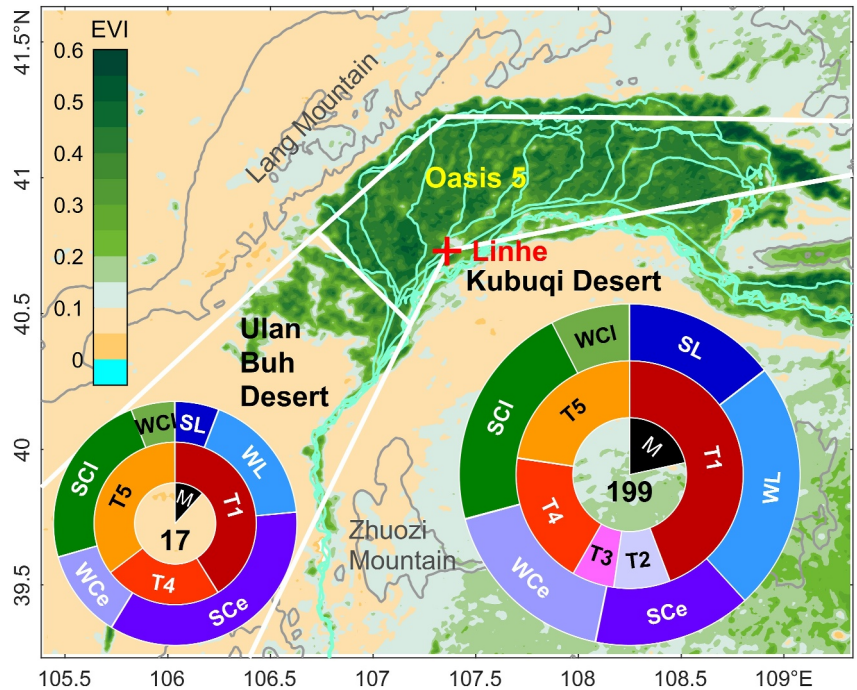

Figure 7. Proportions of organizational modes (outer annuli in the pie chart), synoptic patterns (inner annuli), and far downstream-moving convection (black sectors) in two deserts. The shading represents the averaged EVI over the 2012–2023 warm seasons; the red cross denotes the location of Linhe radar; the cyan curves denote the Yellow River; the gray contours represent terrain elevations of 1,500 m and 2,000 m above mean sea level; and the white lines indicate the borders of three subregions. The total number of CSs in each region is given at the center of each pie chart.

formation of thermal circulation and BLCL (Azorin-Molina & Chen, 2009; Bechtold et al., 1991; Estoque, 1962; Rochetin et al., 2017). However, once BLCL forms and initiates convection by chance when the sharp vegetation contrast creates locally favorable conditions that overcome the unfavorable synoptic ones, the CS may easily get intensified and move downstream, influenced by the strong wind and high CAPE. The important role of the strong midlevel mean wind in the downstream movement was also observed in T5, where the second largest midlevel mean wind (Table 1) is consistent with its second largest proportion of downstream movement (Figure 6b).

Most CSs initiated over arid areas, with the highest frequency observed over the Kubuqi Desert (Figure 8a). This aligns with the distribution of clouds in this region (Sato et al., 2007) and the preference for rainfall distribution over locally drier soil moisture (Taylor et al., 2012).

CSs exhibited a dominant eastward movement, with 22.1% moving eastward, 20.6% southeastward, and 19.6% northeastward, at mean speeds of 24.2, 17.6, and 23.3 km hr^{-1}, respectively (Figures 8a, 9a and 9b). The overall mean speed of movement in all directions was 18.8 km hr^{-1}, and strong lines had a slightly higher speed of 20.8 km hr^{-1}, notably slower than the average movement speed of squall lines in East China (~50 km hr^{-1}) (Z. Y. Meng et al., 2013), which is consistent with the generally weak environmental wind on BLCL days. Among the three favorable synoptic patterns, CSs in T1 moved significantly slower than those in T4 and T5, with T1 having a median speed of 12.9 km hr^{-1}, while those in T4 moved the fastest with a median value of 20.7 km hr^{-1} (Figure 10a).

CSs associated with BLCLs over the Kubuqi Desert were predominantly oriented parallel to the dominant vegetation contrast line, which generally runs along the border between the Oasis and the Kubuqi Desert, with 36.2% oriented east-west and 31.7% northeast-southwest (Figure 9c). The largest proportion of northeast-southwest-orientated CSs was found in T5, in comparison to the other four synoptic patterns (Figure 10b). CSs in T1 to T4 tended to be oriented east-west. There was a large proportion of north-south-orientated CSs in T1.

Table 1
Mean Wind at 500 hPa From 2012 to 2023 in the Key Area of CS Over the Kubuqi Desert (the Red Box in Figure 3)

	U (m s^{-1})	V (m s^{-1})	Wind speed (m s^{-1})	Wind direction (°)
T1	3.6	−1.0	3.7	104.7
T2	8.8	−3.4	9.4	111.2
T3	10.4	−5.2	11.6	116.5
T4	6.6	−2.6	7.1	111.5
T5	9.6	−0.01	9.6	90.0

21698996, 2025, 20, Downloaded from https://agupubs.onlinelibrary.wiley.com/doi/10.1029/2025JD044464 by Peking University Health, Wiley Online Library on [03/12/2025]. See the Terms and Conditions (https://onlinelibrary.wiley.com/terms-and-conditions) on Wiley Online Library for rules of use; OA articles are governed by the applicable Creative Commons License

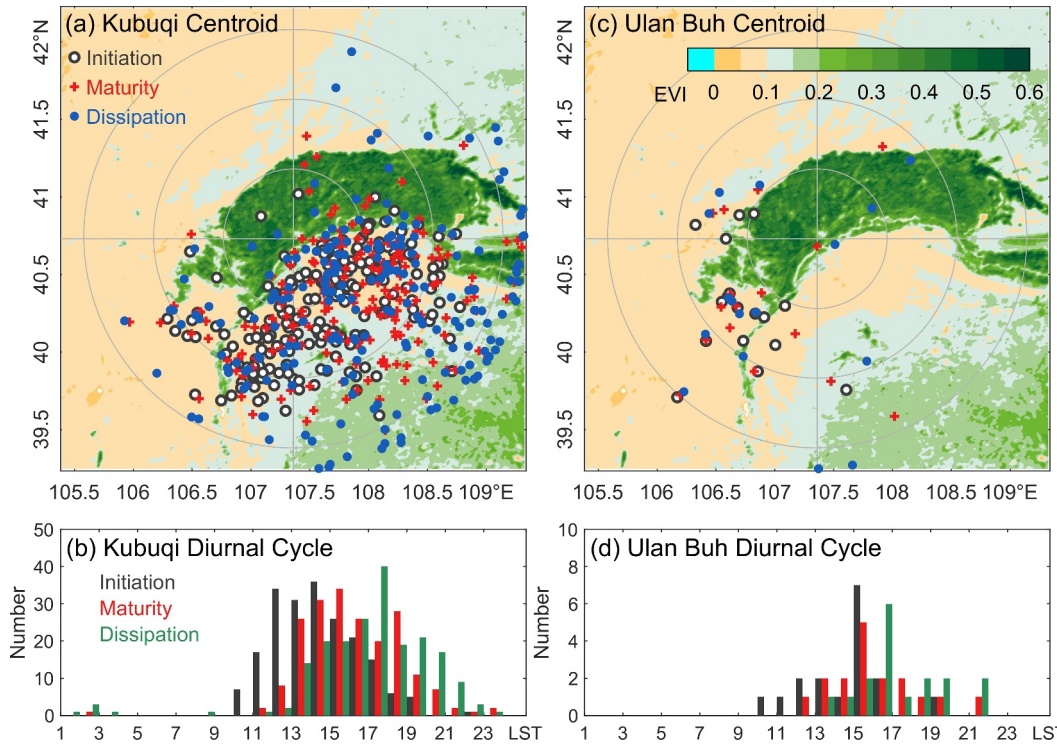

Figure 8. (a) Geographical distribution of centroids at different stages and (b) diurnal cycle for different stages of Kubuqi CSs. Panels (c) and (d) are similar to (a) and (b) but for Ulan Buh CSs. The shading in (a) and (c) represents the averaged EVI over the 2012–2023 warm seasons.

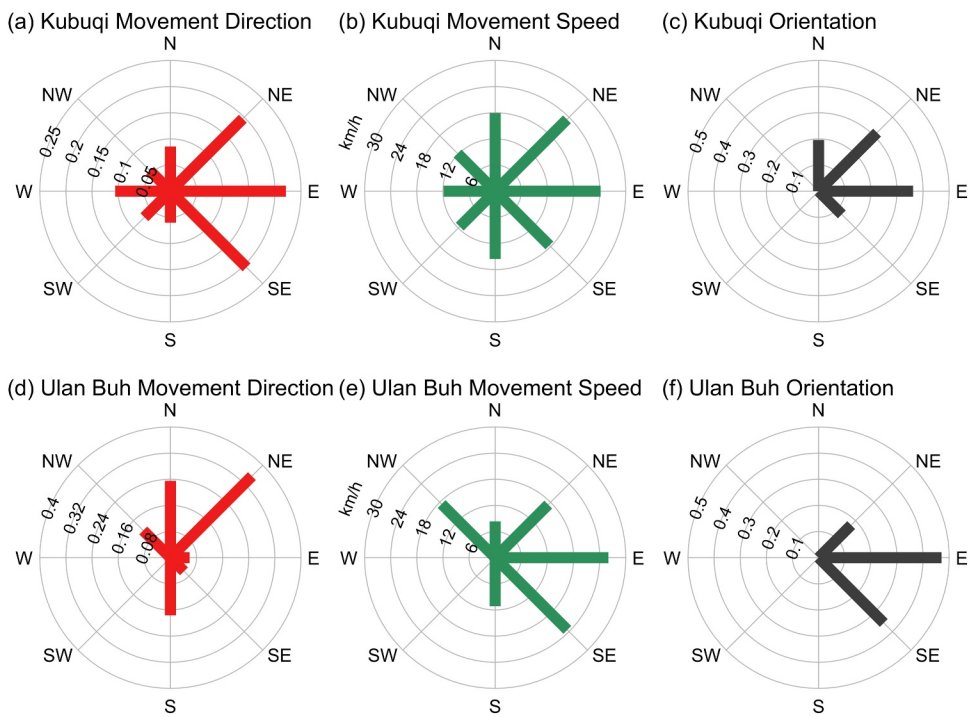

Figure 9. (a) Frequency of movement directions, (b) mean movement speed, and (c) frequency of maturity orientations for Kubuqi CSs. Panels (d–f) are similar to (a–c) but for Ulan Buh CSs.

21698996, 2025, 20, Downloaded from https://agupubs.onlinelibrary.wiley.com/doi/10.1029/2025JD044464 by Peking University Health, Wiley Online Library on [03/12/2025]. See the Terms and Conditions (https://onlinelibrary.wiley.com/terms-and-conditions) on Wiley Online Library for rules of use; OA articles are governed by the applicable Creative Commons License

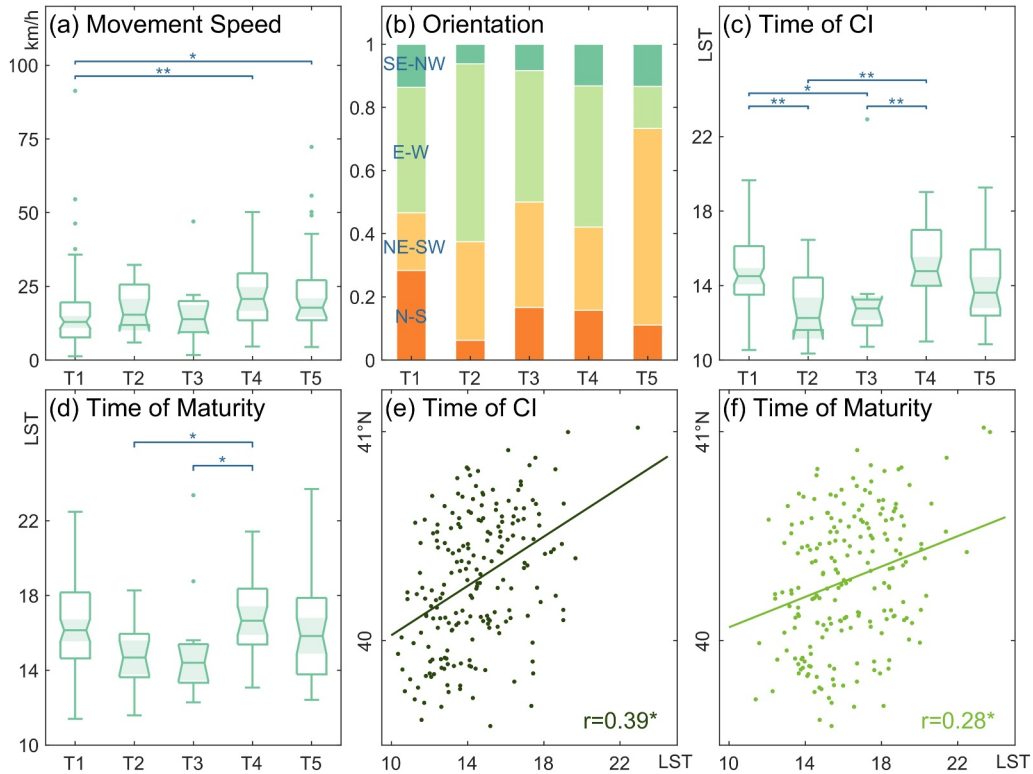

Figure 10. (a) Box-and-whisker plots of movement speed, (b) stacked bars of maturity orientation, and box-and-whisker plots of (c) initiation time and (d) maturity time of Kubuqi CSs. Also given are the meridional distribution of (e) initiation time and (f) maturity time for Kubuqi CSs. The blue lines and asterisks in (a), (c), and (d) indicate the results of the Kruskal-Wallis test, with one, two, and three asterisks representing p-values less than 0.05, 0.01, and 0.001, respectively. The central horizontal line inside each box indicates the median; the top and bottom edges of each box represent the 25th and 75th percentiles; whiskers denote the minimum and maximum values excluding outliers; and dots indicate outliers. The straight lines in (e) and (f) are fitted using the least squares method. The numbers in these two panels are Spearman's correlation coefficients, and the asterisks indicate that they pass the significant test at the 95% confidence level.

CSs in the Hetao area demonstrated a shorter duration and weaker intensity compared to their counterparts in moister environments in China. The duration refers to the period during which the maximum composite reflectivity of CSs remains continuously at least 40 dBZ. Almost all Kubuqi CSs initiated between 1000 and 2000 LST (LST = UTC+8 hr), with two peaks: one at 1200–1300 LST and the other at 1400–1500 LST, approximately 1–3 hr after BLCL formation (Figure 8b). About one half to two hours after initiation, the CSs reached their maximum areas, peaking at 1500–1600 LST. Dissipation peaked around 1800 LST. Approximately 65% of CSs lasted less than 3 hr and 90% less than 6 hr, with a mean duration of 2.6 hr (Figure 11a). Few CSs that did not undergo far downstream movement persisted into the next day.

The life course of CSs initiated under different synoptic patterns and in different parts of the Kubuqi Desert showed slight variations. Relative to unfavorable synoptic patterns T2 and T3, CSs in favorable synoptic patterns T1, T4, and T5 were initiated and matured later (Figures 10c and 10d), with T4 being the latest. This result is surprising and the reasons remain to be explored in the future. In addition, the initiation and maturity times of CSs were positively correlated with the latitude of their initiation positions (Figures 10e and 10f). Zhuozi Mountain (location given in Figure 1) may have facilitated the earlier initiation and development of low-latitude convection in the late morning, while vegetation contrast may have played a more important role in high-latitude convection later at noon or in the afternoon.

The maximum reflectivity of Kubuqi CSs peaked at 55 dBZ with a mean value of 54.7 dBZ (Figure 11b). The mean maximum reflectivity of strong lines in this study was 59.1 dBZ, comparable to the mean maximum reflectivity of squall lines in East China (58−63 dBZ) (Z. Y. Meng et al., 2013). Approximately 70% of CSs produced a maximum area smaller than 100 km^2 and the mean maximum area was 233.4 km^2 (Figure 11c). Two

21698996, 2025, 20, Downloaded from https://agupubs.onlinelibrary.wiley.com/doi/10.1029/2025JD044464 by Peking University Health, Wiley Online Library on [03/12/2025]. See the Terms and Conditions (https://onlinelibrary.wiley.com/terms-and-conditions) on Wiley Online Library for rules of use; OA articles are governed by the applicable Creative Commons License

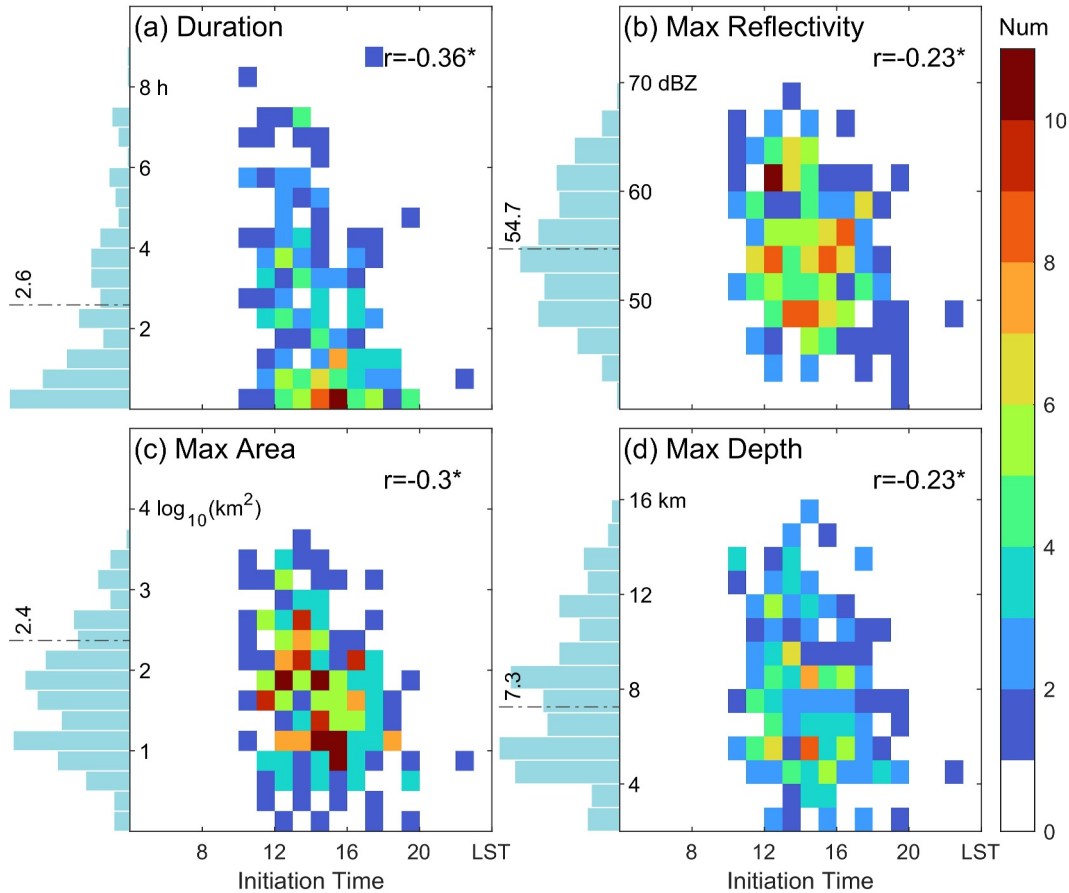

Figure 11. Probability density distributions of (a) duration, (b) maximum reflectivity, (c) maximum area, and (d) maximum depth, with respect to initiation times of Kubuqi CSs. The number in the top-right corner of each subfigure is Spearman's correlation coefficient, with an asterisk indicating statistical significance at the 95% confidence level. Dotted lines indicate the mean values.

peaks in the maximum depth of the CSs, defined as the distance between the base and top of 40 dBZ reflectivity, were observed around 5 and 8 km (Figure 11d). Only 7.0% of CSs developed deeper than 12 km. There was a weak negative correlation between the initiation time of CSs and their duration, intensity, and depth at the 95% confidence level (Figure 11), suggesting that the earlier the CSs initiated, the longer they lasted and the more intense they became.

3.2. CSs Over the Ulan Buh Desert

Relative to CSs over the Kubuqi Desert, significantly fewer BLCL-associated CSs (17 in total) were identified over the Ulan Buh Desert (Figure 7), with the most prevalent organizational mode being strong cell (6 cases). The lower number of samples, particularly in strong line (only 1 case), may be related to the existence of a transition zone (area of $0.15 < \text{EVI} < 0.3$) between the Oasis and the Ulan Buh Desert (Figure 1a) with a weaker EVI gradient.

To quantify surface heterogeneity, EVI gradients were calculated along the borders between the Oasis and both deserts as indicated by the white lines in Figure 1. The mean EVI gradient at the Kubuqi-Oasis border was 0.0136 km^{-1}, while that at the Ulan Buh-Oasis border was only 0.0058 km^{-1}. The weaker vegetation contrast and thus the weaker temperature gradient between the Ulan Buh Desert and the Oasis likely led to reduced BLCL formation, with only 123 BLCLs identified—approximately a quarter of the number observed over the Kubuqi Desert (Figure 2a), and only 13.8% of BLCLs over this subregion were associated with CSs, which was considerably lower than the convective BLCLs ratio over the Kubuqi Desert (Figure 2b).

21698996, 2025, 20, Downloaded from https://agupubs.onlinelibrary.wiley.com/doi/10.1029/2025JD044464 by Peking University Health, Wiley Online Library on [03/12/2025]. See the Terms and Conditions (https://onlinelibrary.wiley.com/terms-and-conditions) on Wiley Online Library for rules of use; OA articles are governed by the applicable Creative Commons License

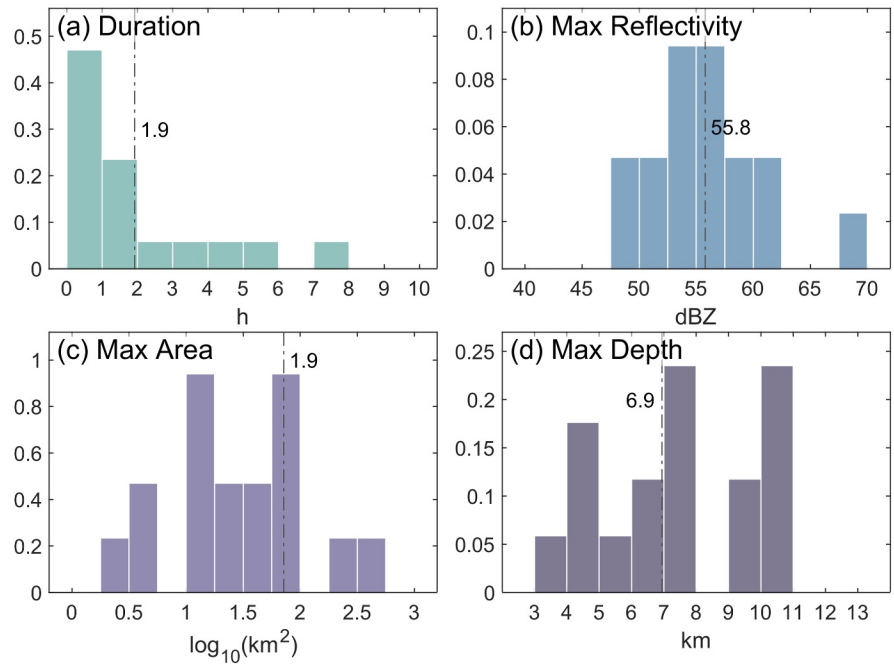

Figure 12. Probability density distributions of (a) duration, (b) maximum reflectivity, (c) maximum area, and (d) maximum depth of Ulan Buh CSs. Dotted lines indicate the mean values.

Similar to CSs over the Kubuqi Desert, the majority of CSs over the Ulan Buh Desert were also initiated over arid areas (Figure 8c). These CSs were primarily oriented east-west (47.0%) and northwest-southeast (35.3%), parallel to their vegetation contrast line (Figure 9f). It is interesting to note that no CSs over the Ulan Buh Desert occurred in T2 and T3 patterns, where the Hetao area is situated behind the 500 hPa trough, and the prevailing low-level wind in the Ulan Buh Desert is northerly (2nd and 3rd rows in Figure 3), which is not conducive to the formation of BLCLs because the formation of Ulan Buh Desert BLCLs primarily relies on the convergence between ambient southerly flows and northerly oasis winds.

Occurring in synoptic patterns with prevailing southerly winds in the low-level atmosphere, Ulan Buh CSs—almost half of which were cellular—tended to move northward (23.5%) and northeastward (35.3%), with the former moving at a lower speed of 8.3 km hr^{-1} and the latter at 17.2 km hr^{-1} (Figures 9d and 9e). This movement feature differed from the eastward trajectory of CSs associated with BLCLs over the Kubuqi Desert. The mean movement speed in all directions was 15.0 km hr^{-1}, slightly lower than that observed for Kubuqi CSs. Only two CSs moved far downstream in a southward direction: one was a strong line and the other was a strong cluster.

CSs over the Ulan Buh Desert initiated relatively later, exhibited a shorter lifespan, and were less organized than those associated with BLCLs over the Kubuqi Desert. This discrepancy may be attributed to the less sharp contrast between the Oasis and the Ulan Buh Desert. All CSs were initiated between 1000 and 2000 LST, with a peak occurring at 1500–1600 LST (Figure 8d). CSs underwent rapid maturation and dissipation following CI, with maturity peaking at 1500–1600 LST and dissipation peaking at 1600–1700 LST. Consequently, the mean duration of Ulan Buh CSs was only 1.9 hr and the median value was only 1 hr (Figure 12a).

The less organized CSs led to their weaker intensity. Although the maximum reflectivity also peaked around 55 dBZ, with a mean value of 55.8 dBZ (Figure 12b), the mean maximum area produced at the CSs maturity stage was 71.7 km^2 (Figure 12c), which was considerably less than that of Kubuqi CSs. The mean maximum depth was 6.9 km (Figure 12d), which was also less than the mean maximum depth of 7.3 km observed in Kubuqi CSs.

3.3. CSs Over the Oasis and Mixed CSs

CSs associated with the BLCLs over the Oasis were few in number, weak in intensity, and all dissipated within the radar range. All five cases exhibited a lack of organization and tended to move either southward or northward

21698996, 2025, 20, Downloaded from https://agupubs.onlinelibrary.wiley.com/doi/10.1029/2025JD044464 by Peking University Health, Wiley Online Library on [03/12/2025]. See the Terms and Conditions (https://onlinelibrary.wiley.com/terms-and-conditions) on Wiley Online Library for rules of use; OA articles are governed by the applicable Creative Commons License

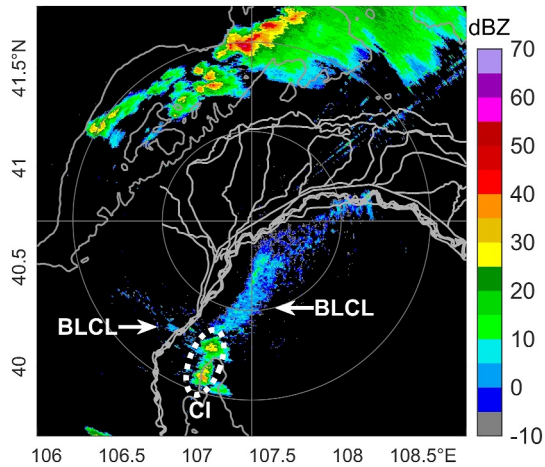

Figure 13. Composite reflectivity from the Linhe radar at 1301 LST on 28 July 2014.

during their relatively short lifespan. Three of them occurred in favorable synoptic patterns, while the other two occurred in unfavorable patterns.

CSs associated with two BLCLs over different subregions, classified as mixed, exhibited great strength, displaying characteristics comparable to those observed in CSs over the Kubuqi Desert. All seven CSs occurred in favorable synoptic patterns, similar to Ulan Buh CSs. Six CSs were classified as strong modes and three of them moved far downstream.

Notably, five mixed CSs were initiated by a BLCL over the Kubuqi Desert and a BLCL over the Ulan Buh Desert, as illustrated in Figure 13. In this instance, two BLCLs formed in a V-shaped configuration to the north of Zhuozi Mountain, with one extending northeast over the Kubuqi Desert and the other extending northwest over the Ulan Buh Desert. When environmental conditions were conducive and the BLCLs were sufficiently intense, the CS initiated near the apex of the V shape and proceeded in a northeast or eastward direction. The formation of these V-shaped BLCLs was closely related to the blocking effect of Zhuozi Mountain on the prevailing southerly winds (Liu, 2023). Such V-shaped BLCLs were frequent in the Hetao area. However, the CSs forming at the apex of V-shaped BLCLs are rare, possibly because of the weak BLCL over the Ulan Buh Desert resulting from the weaker sharpness of the vegetation contrast. Interestingly, the CSs that formed at the apex of V-shaped BLCLs were more impactful (Table 2). All five identified cases are strong-type modes occurring in favorable synoptic conditions, with two moving downstream, representing 40% of occurrences.

4. Conclusions

A statistical analysis of BLCL-associated CSs was conducted in the Hetao area, a region characterized by a sharp vegetation contrast between the Oasis and the surrounding deserts in China. The analysis covered the period from June to August, spanning 2012 to 2023, and was based on radar data at Linhe. In total, 228 CSs were objectively identified, tracked, and categorized into three subregions according to the location of their parent BLCLs. Of the 228 BLCL-initiated CSs, 199 occurred in the Kubuqi Desert, representing nearly 40 times the number observed in the Oasis. In contrast, the Ulan Buh Desert witnessed only 17 CSs, possibly due to the much weaker oasis-desert contrast.

The CSs predominantly initiated over arid areas in the early afternoon, aligning along the dominant vegetation contrast line, with approximately 20% moving far downstream beyond the 166.5-km range of the Linhe radar. Kubuqi CSs typically initiated around 1100–1500 LST with earlier initiation observed at lower latitudes than higher latitudes, moved eastward and lasted 2.6 hr on average. In contrast, Ulan Buh CSs initiated later with a shorter mean duration and moved northward and northeastward at a relatively slower speed.

The CSs were classified into six organizational modes based on their morphology and intensity. Approximately 35% of CSs exhibited linear modes (strong line and weak line, mainly parallel to their parent BLCLs) due to the linear lifting mechanism of BLCL, and 50% were classified as strong modes (strong line, strong cell, and strong cluster). Strong lines demonstrated the greatest downstream propagation (over two thirds). Two fifths of the CSs over the Kubuqi Desert were linear, with the largest proportion of strong line observed among the three

Table 2
Characteristics of Mixed CSs Associated With V-Shaped BLCLs

Date	Synoptic pattern	Organization	Whether to move downstream
29 June 2013	T1	Strong Cluster	Yes
27 July 2014	T5	Strong Cluster	No
28 July 2014	T1	Strong Cell	No
17 July 2018	T1	Strong Cell	No
16 July 2021	T4	Strong Cluster	Yes

21698996, 2025, 20, Downloaded from https://agupubs.onlinelibrary.wiley.com/doi/10.1029/2025JD044464 by Peking University Health, Wiley Online Library on [03/12/2025]. See the Terms and Conditions (https://onlinelibrary.wiley.com/terms-and-conditions) on Wiley Online Library for rules of use; OA articles are governed by the applicable Creative Commons License

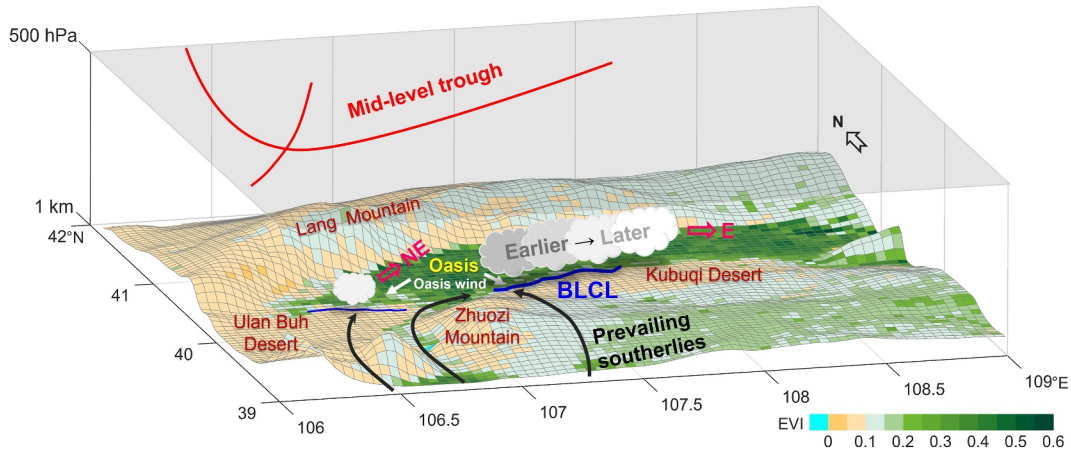

Figure 14. Schematic diagram of the characteristics of BLCL-associated CSs over the Kubuqi versus Ulan Buh deserts in T5 synoptic pattern where the irrigated oasis is positioned ahead of a midlevel trough. The blue lines denote the BLCL. The red lines denote the 500-hPa trough. The black and white arrows denote the near surface wind. The red empty arrows denote the directions of the movement of CSs.

subregions, resulting in more than one fifth of CSs developing downstream. In contrast to weak line over the Kubuqi Desert, the predominant organizational mode of CSs over the Ulan Buh Desert was strong cell.

Among the five synoptic patterns identified in Huang et al. (2022), CSs were more likely to occur in T1, T5, and T4, where the Hetao area experienced both synoptic-scale and mesoscale lifting environments in front of the midlevel westerly trough and over the low-level convergence line. Strong line, which was the organizational mode most likely to develop downstream, showed a preference for T5, where the Hetao area is located in front of a deep midlevel trough with high CAPE. Strong cells were more prevalent in T1 and T4 and equally less frequent in the other three synoptic patterns. All Ulan Buh CSs were observed in favorable synoptic patterns T1, T4, and T5. In contrast, over the Kubuqi Desert, in addition to the dominant CSs in T1, T4, and T5, BLCL-associated CSs may still form in unfavorable T2 and T3 patterns, where the Hetao area is located behind a midlevel trough, especially in T3 with the highest proportion of downstream movement, which warrants further investigation. In addition, three of the five cases in the Oasis occurred in favorable synoptic patterns.

Figure 14 summarizes the contrasting characteristics of CSs over the Kubuqi and the Ulan Buh deserts in the synoptic condition of T5. The Kubuqi Desert exhibited more numerous, intense, and linearly organized CSs, possibly due to its more and stronger BLCLs due to a sharper vegetation contrast with the Oasis, relative to the transitional zone between the Ulan Buh Desert and the Oasis. These hypotheses could be examined using idealized and/or real-world simulations by varying vegetation and thermodynamic contrasts. Additionally, the earlier initiation of CSs at lower latitudes over the Kubuqi Desert suggests an influence of Zhuozi Mountain, which could be explored through sensitivity experiments by modifying the mountain height, location, or shape.

This study provides actionable guidance for enhancing severe convection nowcasting in the Hetao area and downstream regions. Nowcasting operations should prioritize real-time monitoring of the Kubuqi Desert between 1100 and 1500 LST—where 87% of BLCL-initiated storms develop—utilizing high-resolution radar scanning along vegetation-desert boundaries to detect emerging strong line systems. Upon identification, immediate downstream propagation alerts must be issued for these linear systems, especially during T5 synoptic pattern. For the Ulan Buh Desert, nowcasting efforts should focus on delayed-initiation strong cell development. To optimize predictions, nowcasting algorithms should incorporate: (a) BLCL density maps linked to vegetation gradients for initiation hotspot anticipation, (b) organizational mode classifiers prioritizing strong line mobility, and (c) synoptic pattern triggers (escalating alerts for T1/T4/T5; secondary monitoring for T2/T3). Cross-regional data sharing and tiered warning protocols are essential during high-risk T1/T4/T5 patterns, while persistent storm risks under unfavorable T2/T3 conditions over Kubuqi necessitate sustained vigilance. Particular attention should be paid to T3 where even though BLCL and CI occur rarely, they, however, tend to have high downstream impact once they indeed occur. Furthermore, thermal heterogeneity of oasis-desert underlying surfaces regulates storm initiation and development, highlighting the need to refine the land surface parameterization scheme in numerical

21698996, 2025, 20, Downloaded from https://agupubs.onlinelibrary.wiley.com/doi/10.1029/2025JD044464 by Peking University Health, Wiley Online Library on [03/12/2025]. See the Terms and Conditions (https://onlinelibrary.wiley.com/terms-and-conditions) on Wiley Online Library for rules of use; OA articles are governed by the applicable Creative Commons License

models. These operational enhancements may substantially extend critical nowcasting lead times for both local and downstream areas.

This study unveiled the general characteristics of CSs associated with BLCLs over a heterogeneously vegetated underlying surface resulting from a historically large anthropogenic irrigation project adjacent to extensive deserts and mountains. Vegetation contrast is known to vary with seasonal change, deforestation or afforestation, and climate change. The extent to which BLCLs and their associated storms may vary with climate and environmental changes, as well as whether the oasis and desert land surface features may feed back from the BLCL-associated storms and precipitation, are interesting questions worthy of exploring in the future.

Conflict of Interest

The authors declare no conflicts of interest relevant to this study.

Data Availability Statement

The radar data were provided by the National Meteorological Information Center of the China Meteorological Administration (https://data.cma.cn/data/cdcindex/cid/0b9164954813c573.html). The MODIS data (MOD13A3-V061, Didan, 2021) were downloaded from NASA's Earth Observing System Data and Information System (EOSDIS; https://search.earthdata.nasa.gov/search). The ASTER Global Digital Elevation Model (ASTGTM-V003, NASA/METI/AIST/Japan Spacesystems and U.S./Japan ASTER Science Team, 2019) was also downloaded from EOSDIS. The TITAN and related components were downloaded from NCAR's github (https://github.com/ncar/lrose-core).

Acknowledgments
This study was sponsored by the National Natural Science Foundation of China (Grants 42030604) and Natural Science Foundation of Fujian Province (Grants 2023J011338).

References

Azorin-Molina, C., & Chen, D. (2009). A climatological study of the influence of synoptic-scale flows on sea breeze evolution in the Bay of Alicante (Spain). *Theoretical and Applied Climatology*, *96*(3), 249–260. https://doi.org/10.1007/s00704-008-0028-2

Barton, E. J., Taylor, C. M., Klein, C., Harris, P. P., & Meng, X. (2021). Observed soil moisture impact on strong convection over mountainous Tibetan Plateau. *Journal of Hydrometeorology*, *22*(3), 561–572. https://doi.org/10.1175/JHM-D-20-0129.1

Bechtold, P., Pinty, J.-P., & Mascart, F. (1991). A numerical investigation of the influence of large-scale winds on sea-breeze- and inland-breeze-type circulations. *Journal of Applied Meteorology and Climatology*, *30*(9), 1268–1279. https://doi.org/10.1175/1520-0450(1991)030<1268:ANIOTI>2.0.CO;2

Chug, D., Dominguez, F., Taylor, C. M., Klein, C., & Nesbitt, S. W. (2023). Dry-to-wet soil gradients enhance convection and rainfall over subtropical South America. *Journal of Hydrometeorology*, *24*(9), 1563–1581. https://doi.org/10.1175/JHM-D-23-0031.1

Courault, D., Drobinski, P., Brunet, Y., Lacarrere, P., & Talbot, C. (2007). Impact of surface heterogeneity on a buoyancy-driven convective boundary layer in light winds. *Boundary-Layer Meteorology*, *124*(3), 383–403. https://doi.org/10.1007/s10546-007-9172-y

Didan, K. (2021). Modis/Terra vegetation indices monthly L3 global 1km sin grid (Version 6.1) [Dataset]. *NASA Land Processes Distributed Active Archive Center*. https://doi.org/10.5067/MODIS/MOD13A3.061

Dixon, M., & Wiener, G. (1993). TITAN: Thunderstorm identification, tracking, analysis, and nowcasting - A radar-based methodology. *Journal of Atmospheric and Oceanic Technology*, *10*(6), 785–797. https://doi.org/10.1175/1520-0426(1993)010<0785:ttitaa>2.0.co;2

Dwyer, J., & Schmidt, G. (2006). The MODIS reprojection tool [Software]. *Earth science satellite remote sensing*. In J. J. Qu, W. Gao, M. Kafatos, R. E. Murphy, & V. V. Salomonson (Eds.). Springer. Berlin, Heidelberg. https://doi.org/10.1007/978-3-540-37294-3_9

Estoque, M. A. (1962). The sea breeze as a function of the prevailing synoptic situation. *Journal of the Atmospheric Sciences*, *19*(3), 244–250. https://doi.org/10.1175/1520-0469(1962)019<0244:TSBAAF>2.0.CO;2

Houze, R. A. (2004). Mesoscale convective systems. *Reviews of Geophysics*, *42*(4), RG4003. https://doi.org/10.1029/2004rg000150

Huang, Y., Meng, Z., Li, W., Bai, L., & Meng, X. (2019). General features of radar-observed boundary layer convergence lines and their associated convection over a sharp vegetation-contrast area. *Geophysical Research Letters*, *46*(5), 2865–2873. https://doi.org/10.1029/2018gl081714

Huang, Y., Meng, Z., & Zhang, M. (2022). Synoptic impacts on the occurrence of mesoscale boundaries and their associated convection over an area of sharp vegetation contrast. *Geophysical Research Letters*, *49*(16), e2022GL099449. https://doi.org/10.1029/2022GL099449

Kawase, H., Yoshikane, T., Hara, M., Kimura, F., Sato, T., & Ohsawa, S. (2008). Impact of extensive irrigation on the formation of cumulus clouds. *Geophysical Research Letters*, *35*(1), L01806. https://doi.org/10.1029/2007gl032435

Lee, J. M., Zhang, Y., & Klein, S. A. (2019). The effect of land surface heterogeneity and background wind on shallow cumulus clouds and the transition to deeper convection. *Journal of the Atmospheric Sciences*, *76*(2), 401–419. https://doi.org/10.1175/jas-d-18-0196.1

Liu, H. (2023). *Distribution characteristics and influenced mechanism of convection initiation over a real-world sharp vegetation-contrast area in the Hetao area of Inner Mongolia*. (Doctoral dissertation). Peking University. Beijing, China.

Liu, H., Meng, Z., Zhu, Y., & Huang, Y. (2023). Convection initiation associated with a boundary layer convergence line over a real-world sharp vegetation-contrast area. *Monthly Weather Review*, *151*(5), 1189–1212. https://doi.org/10.1175/MWR-D-22-0083.1

Meng, X., Sun, Y., Sarina, Yuan, H., & Hasi (2013). Correlation between eastward developing of hetao cyclone and the severe rainstorm in Beijing on 21 July 2012. *Meteorological Monthly*, *39*(12), 1542–1549. https://doi.org/10.7519/j.issn.1000-0526.2013.12.002

Meng, Z., Meng, X., Wang, C., Huang, Y., Zhang, S., Liu, H., et al. (2024). Desert–oasis convergence line and deep convection experiment (DECODE). *Bulletin of the American Meteorological Society*, *105*(12), E2355–E2384. https://doi.org/10.1175/BAMS-D-23-0222.1

Meng, Z. Y., Yan, D. C., & Zhang, Y. J. (2013). General features of squall lines in East China. *Monthly Weather Review*, *141*(5), 1629–1647. https://doi.org/10.1175/mwr-d-12-00208.1

21698996, 2025, 20, Downloaded from https://agupubs.onlinelibrary.wiley.com/doi/10.1029/2025JD044464 by Peking University Health, Wiley Online Library on [03/12/2025]. See the Terms and Conditions (https://onlinelibrary.wiley.com/terms-and-conditions) on Wiley Online Library for rules of use; OA articles are governed by the applicable Creative Commons License

Meng, Z. Y., & Zhang, Y. J. (2012). On the squall lines preceding landfalling tropical cyclones in China. *Monthly Weather Review*, *140*(2), 445–470. https://doi.org/10.1175/mwr-d-10-05080.1

Parker, M. D., & Johnson, R. H. (2000). Organizational modes of midlatitude mesoscale convective systems. *Monthly Weather Review*, *128*(10), 3413–3436. https://doi.org/10.1175/1520-0493(2001)129<3413:omommc>2.0.co;2

Rochetin, N., Couvreux, F., & Guichard, F. (2017). Morphology of breeze circulations induced by surface flux heterogeneities and their impact on convection initiation. *Quarterly Journal of the Royal Meteorological Society*, *143*(702), 463–478. https://doi.org/10.1002/qj.2935

Sato, T., Kimura, F., & Hasegawa, A. S. (2007). Vegetation and topographic control of cloud activity over arid/semiarid Asia. *Journal of Geophysical Research*, *112*(D24), D24109. https://doi.org/10.1029/2006jd008129

Seth, A., & Giorgi, F. (1996). Three-dimensional model study of organized mesoscale circulations induced by vegetation. *Journal of Geophysical Research*, *101*(D3), 7371–7391. https://doi.org/10.1029/95jd02677

Smith, B. T., Thompson, R. L., Grams, J. S., Broyles, C., & Brooks, H. E. (2012). Convective modes for significant severe thunderstorms in the contiguous United States. Part I: Storm classification and climatology. *Weather and Forecasting*, *27*(5), 1114–1135. https://doi.org/10.1175/waf-d-11-00115.1

Taylor, C. M. (2015). Detecting soil moisture impacts on convective initiation in Europe. *Geophysical Research Letters*, *42*(11), 4631–4638. https://doi.org/10.1002/2015gl064030

Taylor, C. M., de Jeu, R. A. M., Guichard, F., Harris, P. P., & Dorigo, W. A. (2012). Afternoon rain more likely over drier soils. *Nature*, *489*(7416), 423–426. https://doi.org/10.1038/nature11377

Taylor, C. M., Gounou, A., Guichard, F., Harris, P. P., Ellis, R. J., Couvreux, F., & De Kauwe, M. (2011). Frequency of Sahelian storm initiation enhanced over mesoscale soil-moisture patterns. *Nature Geoscience*, *4*(7), 430–433. https://doi.org/10.1038/ngeo1173

NASA/METI/AIST/Japan Spacesystems and U.S./Japan ASTER Science Team. (2019). Aster global digital elevation model (Version 3) [Dataset]. *NASA Land Processes Distributed Active Archive Center*. https://doi.org/10.5067/ASTER/ASTGTM.003

Wang, C., Tian, W. S., Parker, D. J., Marsham, J. H., & Guo, Z. H. (2011). Properties of a simulated convective boundary layer over inhomogeneous vegetation. *Quarterly Journal of the Royal Meteorological Society*, *137*(654), 99–117. https://doi.org/10.1002/qj.724

Yu, H. Z., & Meng, Z. Y. (2016). Key synoptic-scale features influencing the high-impact heavy rainfall in Beijing, China, on 21 July 2012. *Tellus Series a-Dynamic Meteorology and Oceanography*, *68*(1), 31045. https://doi.org/10.3402/tellusa.v68.31045

Yu, X. (2012). Investigation of Beijing extreme flooding event on 21 July 2012. *Meteorological Monthly*, *38*(11), 1313–1329. https://doi.org/10.7519/j.issn.1000-0526.2012.11.001

Yuan, S. S., Wang, Y. C., Quiring, S. M., Ford, T. W., & Houston, A. L. (2020). A sensitivity study on the response of convection initiation to in situ soil moisture in the central United States. *Climate Dynamics*, *54*(3–4), 2013–2028. https://doi.org/10.1007/s00382-019-05098-0

21698996, 2025, 20, Downloaded from https://agupubs.onlinelibrary.wiley.com/doi/10.1029/2025JD044464 by Peking University Health, Wiley Online Library on [03/12/2025]. See the Terms and Conditions (https://onlinelibrary.wiley.com/terms-and-conditions) on Wiley Online Library for rules of use; OA articles are governed by the applicable Creative Commons License